BJ www.biochemj.org

Biochem. J. (2011) **436**, 341–350 (Printed in Great Britain) doi:10.1042/BJ20102090

Substrate diffusion and oxidation in GMC oxidoreductases: an experimental and computational study on fungal aryl-alcohol oxidase

Aitor HERNÁNDEZ-ORTEGA*[1], Kenneth BORRELLI†[1], Patricia FERREIRA‡, Milagros MEDINA‡, Angel T. MARTÍNEZ*[2] and Victor GUALLAR†[2]

*Centro de Investigaciones Biológicas, Consejo Superior de Investigaciones Científicas (CSIC), Ramiro de Maeztu 9, E-28040 Madrid, Spain, †Catalan Institution for Research and Advanced Studies, Barcelona Supercomputing Center, Edificio Nexus II, E-08028 Barcelona, Spain, and ‡Department of Biochemistry and Molecular and Cellular Biology and Institute of Biocomputation and Physics of Complex Systems, University of Zaragoza, E-50009 Zaragoza, Spain

AAO (aryl-alcohol oxidase) provides H_2O_2 in fungal degradation of lignin, a process of high biotechnological interest. The crystal structure of AAO does not show open access to the active site, where different aromatic alcohols are oxidized. In the present study we investigated substrate diffusion and oxidation in AAO compared with the structurally related CHO (choline oxidase). Cavity finder and ligand diffusion simulations indicate the substrate-entrance channel, requiring side-chain displacements and involving a stacking interaction with Tyr^{92}. Mixed QM (quantum mechanics)/MM (molecular mechanics) studies combined with site-directed mutagenesis showed two active-site catalytic histidine residues, whose substitution strongly decreased both catalytic and transient-state reduction constants for *p*-anisyl alcohol in the H502A (over 1800-fold) and H546A (over 35-fold) variants. Combination of QM/MM energy profiles, protonation predictors, molecular dynamics, mutagenesis and pH profiles provide a robust answer regarding the nature of the catalytic base. The histidine residue in front of the FAD ring, AAO His^{502} (and CHO His^{466}), acts as a base. For the two substrates assayed, it was shown that proton transfer preceded hydride transfer, although both processes are highly coupled. No stable intermediate was observed in the energy profiles, in contrast with that observed for CHO. QM/MM, together with solvent KIE (kinetic isotope effect) results, suggest a non-synchronous concerted mechanism for alcohol oxidation by AAO.

Key words: aryl-alcohol oxidase (AAO), catalytic base, glucose-methanol-choline oxidase (GMC) oxidoreductase, molecular docking, quantum mechanics/molecular mechanics (QM/MM), reaction mechanism.

INTRODUCTION

AAO (aryl-alcohol oxidase; EC 1.1.3.7) catalyses the oxidation of aromatic, and some aliphatic polyunsaturated, alcohols with the concomitant production of H_2O_2 [1] involved in lignin biodegradation in a reaction catalysed by high-redox-potential peroxidases [2]. Lignin removal is a key step for carbon recycling in land ecosystems, and a key issue for the industrial use of plant biomass in lignocellulose biorefineries, where biotechnology will contribute to the sustainable production of biofuels, chemicals and other products [3]. The overall AAO reaction involves a polyunsaturated alcohol, with a primary hydroxy group at the α-carbon, and O_2 in the presence of a FAD enzyme cofactor:

$$\text{alcohol} + O_2 \xrightarrow{\text{AAO-FAD}} \text{aldehyde} + H_2O_2 \quad (1)$$

After gene cloning [4], homology modelling of AAO revealed common features with members of the GMC (glucose-methanol-choline oxidase) superfamily of oxidoreductases [5]. One of the similarities with some of these FAD-containing enzymes is the presence of two conserved histidine residues involved in catalysis, His^{502} and His^{546} in *Pleurotus eryngii* AAO. The importance of these AAO histidine residues in the enzymatic process has been shown by mutational studies [6]. The crystal structure for *P. eryngii* AAO (PDB code 3FIM) has recently been obtained [7], confirming the catalytically relevant positions of His^{502} and His^{546}, right in the vicinity of the FAD cofactor (Figure 1, left-hand side) and the structural relationship of AAO with CHO (choline oxidase). One of the questions that arises from the inspection of the crystal structure is the entrance of large ligands into the active site. The structure does not present an obvious entrance channel, and the packing in the active site appears quite compact. In particular, Tyr^{92} blocks access to the catalytic N-5 of the isoalloxazine ring of AAO FAD, requiring large residue reorganization upon ligand entrance.

In the GMC superfamily, the most accepted catalytic mechanism starts with a proton abstraction from an alcohol substrate by an active-site base, which could correspond to the above-mentioned His^{502} or His^{546} in *P. eryngii* AAO and to His^{466} (or His^{351}) in *Arthrobacter globiformis* CHO (Figure 1), followed by hydride transfer to the FAD N-5. The process continues by O_2 reduction to H_2O_2 by FAD. Mechanistic studies based on substrate KIEs (kinetic isotope effects) in CHO and methanol oxidase proposed the existence of two distinct steps in the reductive half-reaction, with the rate-limiting step being the hydride transfer from a protein-stabilized substrate alkoxide [8,9]. Mutational studies on CHO [10–12] have aimed to address the role of the active-site residues in the catalytic process. Both His^{466} and His^{351} are important for the alcohol proton abstraction, although there is

Abbreviations used: AAO, aryl-alcohol oxidase; APBS, Adaptive Poisson Boltzmann Solver; CHO, choline oxidase; GMC, glucose-methanol-choline oxidase; ICDA, Interaction Cluster Decomposition Algorithm; KIE, kinetic isotope effect; MD, molecular dynamics; MM, molecular mechanics; PELE, Protein Energy Landscape Exploration; QM, quantum mechanics.

[1] These authors contributed equally to this work.
[2] Correspondence may be addressed to either of these authors (email atmartinez@cib.csic.es or victor.guallar@bsc.es).

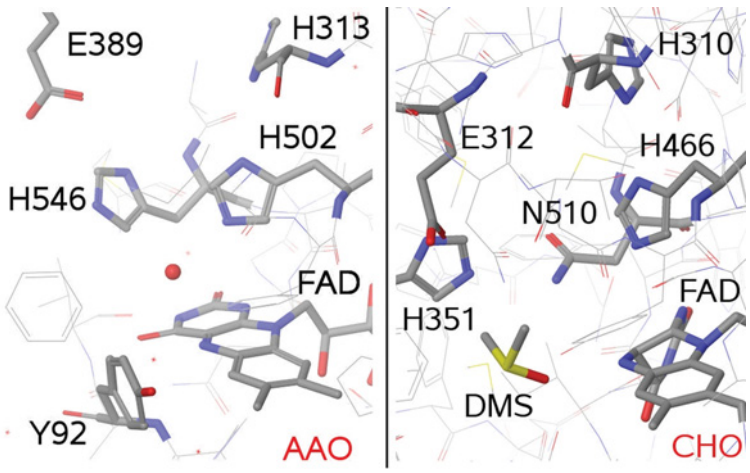

Figure 1 Active site in AAO and CHO crystal structures

The FAD isoalloxazine ring and five active-site residues are shown (as CPK sticks). A dimethyl sulfoxide (DMS) molecule occupies the CHO substrate-binding site, whereas a water molecule (red sphere) is found at the putative active site of AAO. From PDB codes 3FIM and 2JBV respectively [7,11].

not a clear picture of the identity of the base; additionally, Glu^{312} appears to be important for substrate binding by CHO.

Computer simulations, and mechanistic and site-directed mutagenesis experiments have been used in the present study to investigate the structural basis for the migration of *p*-anisyl alcohol, the natural AAO substrate [13], and 2,4-hexadien-1-ol, a structurally different AAO substrate [1], into the active site, and the hydride (and proton) transfer reaction during catalysis. For the sake of comparison, simulations of choline oxidation by the related CHO are also presented. Ligand migration and induced fit were simulated with PELE (Protein Energy Landscape Exploration) [14], a recently developed methodology capable of modelling protein–ligand recognition mechanisms. To obtain a description of the oxidation mechanism, we used mixed QM (quantum mechanics)/MM (molecular mechanics) methods that combine a classical region, described by a set of 'solid' spheres with point charges and classical force fields, with a quantum region where the Schrödinger equation is solved. Thus the explicit electronic description of the system is limited to the QM region covering all of the atoms involved in the biochemical process [15,16].

MATERIALS AND METHODS

Enzyme and mutated variants

Recombinant AAO of *P. eryngii* was obtained by *Escherichia coli* expression of the mature AAO cDNA (GenBank® accession number AF064069) followed by *in vitro* activation [17]. AAO variants were prepared using the QuikChange® site-directed mutagenesis kit (Stratagene). For the PCR, the AAO cDNA cloned into the pFLAG1 vector was used as template, together with oligonucleotides bearing the required mutations (see the Supplementary Experimental section at http://www.BiochemJ.org/bj/436/bj4360341add.htm). Mutations were confirmed by sequencing (GS-FLX sequencer from Roche) and the mutated variants were produced [17]. Enzyme concentrations were determined using molar absorption coefficients: AAO, ε_{463} 11050 $M^{-1} \cdot cm^{-1}$; H502S, ε_{468} 9980 $M^{-1} \cdot cm^{-1}$; H502A, ε_{467} 9800 $M^{-1} \cdot cm^{-1}$; H546S ε_{463} 12400 $M^{-1} \cdot cm^{-1}$; and H546A, ε_{467} 9669 $M^{-1} \cdot cm^{-1}$.

Steady-state and transient-state kinetic measurements

Enzyme activity under steady-state conditions was monitored spectrophotometrically by linear-phase oxidation of *p*-anisyl alcohol (from Sigma–Aldrich) to *p*-anisaldehyde (ε_{285} 16950 $M^{-1} \cdot cm^{-1}$) [1]. Kinetic constants were determined by varying simultaneously the concentration of *p*-anisyl alcohol and O_2 in 0.1 M phosphate (pH 6 at 25 °C), for the wild-type AAO, and H546S and H546A variants (for details see the Supplementary Experimental section). For the H502S and H502A variants, the steady-state constants were determined only by varying the alcohol concentration under air-saturated buffer, since the (low) enzyme turnover rates were independent of the O_2 concentration, and the constants were obtained by fitting the initial rate data to the Michaelis–Menten equation. pH-dependence of steady-state kinetic constants in AAO-mutated variants was studied at 25 °C in air-saturated 0.1 M citrate phosphate for pH 3–7, and 0.1 M pyrophosphate for pH 8–9 (the equations used are given in the Supplementary Experimental section). For transient-state kinetic studies, an Applied Photophysics SX18.MV stopped-flow spectrophotometer, interfaced with an Acorn computer, was used (together with the SX18.MV and Xscan softwares). Reductive half-reactions were analysed under anaerobic conditions [18] at different temperatures, and analyses were performed using the Pro-K software (Applied Photophysics) (see the Supplementary Experimental section).

AAO and CHO model set-up

AAO computational studies were based on the crystal structure with PDB code 3FIM [7]. After visual inspection, His^{91}, His^{313}, His^{387} and His^{398} were protonated in their ε position (termed Hie), and His^{137}, His^{148} and His^{360} were protonated in both their ε and δ positions (termed Hip, positively charged); all other histidine residues were δ protonated (termed Hid). The protonation state of the catalytically active histidine residues, His^{502} and His^{546}, were further studied with MD (molecular dynamics) and QM/MM methods.

For CHO we started from the PDB code 2JBV A-chain holo crystal structure [11]. The side chains of Glu^{222} and Glu^{340} were completed and sampled with PLOP [19]. The oxygen atom forming an adduct with the FAD cofactor [20] was removed

and the crystal substrate analogue DMSO was used to model the cognate choline substrate. After visual inspection, His^{310}, His^{506}, His^{257} and His^{148} were protonated in their ε position and His^{216} and His^{149} were protonated in both their ε and δ positions; all other histidine residues were δ protonated. Owing to the presence of the DMSO molecule, it was not necessary to diffuse the ligand into the active site, as described for AAO. The system was then equilibrated with a 1 ns MD trajectory. After the initial 200 ps in the MD trajectory, the choline substrate adopted a catalytic position, where the alcohol group was in close contact with His^{466}.

Ligand and protein dynamic exploration: PELE

The PELE algorithm combines a steered stochastic approach with protein structure prediction methods, capable of projecting the migration dynamics of ligands in proteins [14,21,22]. The heuristic algorithm of PELE is based on three main steps: (i) ligand and protein local perturbation, including translation and rotation of the ligand, and protein α-carbon displacement following an anisotropic network model approach; (ii) side-chain sampling, by placing all side chains local to the ligand; and (iii) energy minimization, involving the minimization of a region including, at least, all residues local to the atoms involved in (i) and (ii). Typically, a simulation involves several processors running multiple steps and sharing information towards addressing a common task. SiteMap [23] was used for exploring cavities in AAO, and localizing the start point for PELE migrations.

Protonation predictors and MD calculations

Three programs were used to calculate theoretical hydrogen positions and pK_a values of the putative bases: (i) WHAT IF [24], which uses hydrogen-bonding patterns to choose the best protonation state of titratable residues;) (ii) APBS (Adaptive Poisson Boltzmann Solver) [25] to calculate intrinsic pK_a shifts by the surrounding residues in single snapshots using the Poisson–Boltzmann equation; and (iii) ICDA (Interaction Cluster Decomposition Algorithm) [26], which uses rotamer library sampling of clusters of titratable residues scored with a MM force-field and generalized Born implicit solvation.

MD calculations were performed with NAMD version 2.6 [27] starting from structures provided by the previous ligand migration. The proteins were solvated in a 0.5 M NaCl solution in periodic boxes of $90\ \text{Å} \times 80\ \text{Å} \times 70\ \text{Å}$ ($1\ \text{Å} = 0.1$ nm). Each system contained approximately 12 000 water molecules and 46 000 total atoms, and was equilibrated by a minimization followed by 10 ps of MD in the NVT (N, number of atoms; V, volume of the system; T, temperature of the system) ensemble followed by 0.5 ns each in the NPT (P, pressure of the system) and NVT ensembles with a step size of 1 fs. Production runs consisted of 5 ns of MD with a 2 fs step size in the NVT ensemble using the particle mesh Ewald method to treat long-range electrostatics.

QM/MM and QM calculations

All QM/MM calculations were performed with the Qsite program (Schrödinger) using the DFT (density functional theory) B3LYP level of theory, the 6-31G* basis set and the hydrogen-like boundary approximation. Unless noted, the quantum region included: the flavin, the ligand (alcohol substrate), the three active-site histidine residues (His^{502}, His^{313} and His^{546} in AAO and His^{466}, His^{310} and His^{351} in CHO), Glu^{389} in AAO and Gln^{510} in CHO. The OPLS-AA (Optimized Potentials for Liquid Simulations-all atoms) force-field was used for the treatment of the MM part, with a 100 Å non-bonding cut-off. For both enzymes, the QM/MM initial system was obtained after equilibration of an explicit water system with MD and by removing all water molecules beyond 10 Å from the protein surface. All geometry optimizations were performed by harmonically constraining the oxygen atom of the outermost 5 Å of the water layer (beyond 20 Å of any atom in the QM region). Gas-phase second-order MP2 (Moller Plesset) QM calculations were performed using Gaussian03 (Gaussian) with a 6-311G* basis set.

The QM region size (~160 atoms) and methodology (B3LYP) does not allow us to go beyond a QM/MM reaction co-ordinate analysis (geometry optimizations along a proton/hydride reaction co-ordinate). This same level of theory, however, has shown very good agreement in many enzymatic systems [15,16]. When building the QM/MM reaction co-ordinates, the possibility of a proton transfer followed by a hydride transfer and the reverse process have been considered. The *x*-axis is the sum of the proton- and hydride-transfer distances (proton to proton-acceptor distance); large values corresponding to the alcohol reactants and smaller ones to the aldehyde products. For each protonation state (see below) we studied three different mechanisms. The first two involve only one transferred atom being forced to move (either the proton or the hydride) with 0.15 Å increments. The donor-transferred distance is then constrained and the rest of the system is minimized. The third mechanism involves the simultaneous (concerted) movement of both atoms.

RESULTS

Computational and experimental studies were combined to unravel the mechanism of alcohol oxidation at the buried active site of AAO. First, the alcohol-migration pathway from the protein surface was determined using the PELE software after cavity exploration. Then, the role of two active-site histidine residues was experimentally investigated by site-directed mutagenesis, and their protonation states predicted with the purpose of identifying the catalytic base. Finally, energy profiles of the reactions of AAO, and related CHO, were obtained by QM/MM methods to determine the timing of the proton and hydride transfers, and the existence of reaction intermediates.

Ligand migration to the AAO active site

In the AAO crystal structure, the buried active site has only a few water molecules, without a large cavity, and with the access to the catalytic N-5 of the FAD blocked by Tyr^{92} and other residues (Figure 1, left-hand side). Thus direct docking of large ligands, such as AAO aromatic alcohol substrates, does not seem an appropriate procedure. This was confirmed when exploring possible cavities with SiteMap, which could only find binding sites on the protein surface. Thus we proceeded to dock the ligand on the surface for subsequent migration into the active site by PELE. Interestingly, the highest score surface lay in the vicinity of Pro^{402}, next to a flexible loop that connects the surface and the active site. To better characterize the migration entrance, we mutated *in silico* the active-site water molecule shown in Figure 1 into methanol, and performed migration simulations by passing to PELE the task of moving the ligand away from its initial position, with random non-preassigned directions. After three simulations with different Metropolis temperatures (300, 500 and 1000 K), all simulations resulted in the same exit pathway, ending in the SiteMap best scoring surface cavity (Supplementary Figure S1 at http://www.BiochemJ.org/bj/436/bj4360341add.htm).

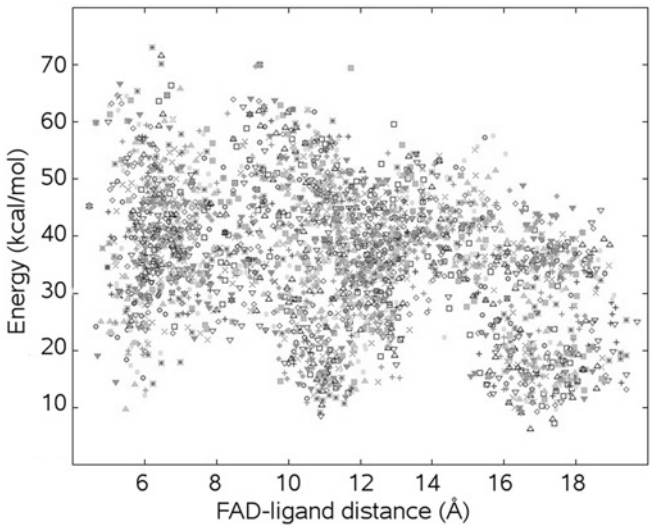

Figure 2 Energy profile for substrate diffusion into the AAO active site obtained with PELE

The *x*-axis shows the distance of the N-5 position of the isoalloxazine ring of FAD to the 2,4-hexadien-1-ol centre of mass, and the *y*-axis shows the internal energies of hundreds of conformations obtained by PELE (points correspond to the different conformations mapped by 12 processors working for 10 h).

The agreement between the surface cavity finder and the methanol expulsion migration clearly points to the entrance of the ligand migration channel. We placed the *p*-anisyl alcohol and 2,4-hexadien-1-ol ligands at this surface point and asked PELE to migrate them towards the active site by setting a common task of shortening the distance with His[502], whose role in catalysis is discussed below. Figure 2 shows the energy profile for this diffusion to the active site for the 2,4-hexadien-1-ol ligand, which was equivalent to the *p*-anisyl alcohol energy profile. The internal energy of hundreds of conformations is plotted against the ligand–FAD distance, and three minima are clearly observed. The energy profile indicates that the entrance is located at a distance of ~17 Å from the isoalloxazine ring, next to Pro[402]. From this point, the motion of the ligand is highly coupled to oscillations of the Gln[395]–Thr[406] loop. The second minimum corresponds to the first stable intermediate at ~11 Å from the isoalloxazine ring of FAD, where it interacts (through a π interaction) with Phe[397]. At this stage, further migration of the ligand to the active site requires side-chain readjustment of this phenylalanine residue, of several hydrophobic residues (such as Leu[315] and Ile[391]) and of Tyr[92]. In the active site, the ligands adopt catalytically active conformations at distances of ~5 Å (ligand centre of mass to N-5) from the isoalloxazine ring.

Figure 3 shows three snapshots along the *p*-anisyl alcohol migration pathway corresponding to the three energy minima shown in Figure 2. Figure 3(A) shows a representative conformation for the surface-docked structure. Figure 3(B) shows the intermediate where the π–π stacking between the substrate *p*-anisyl alcohol and Phe[397] can be clearly observed. Figure 3(C) indicates an active-site conformation, where the the proton and hydride abstraction co-ordinates are indicated with pink lines. This last structure corresponds to the catalytically active species from which the QM/MM and other calculations described below were performed.

The latter structure also suggests that Tyr[92] at the active site would establish π–π stacking interactions with the alcohol substrate. The interaction observed is not a parallel stacking interaction, but an edge-to-face (T-shaped) interaction (Figure 3C). QM MP2 interaction energies, at the final geometries obtained with PELE, confirmed the nature of these stacking interactions. We obtained -2.7 and -1.6 kcal·mol^{-1} (1 kcal = 4.184 kJ) stabilization energies for the *p*-anisyl and 2,4-hexadien-1-ol alcohols respectively.

Additionally, three movies were produced to illustrate the ligand migration into the active site (Supplementary Movies S1–S3 at http://www.BiochemJ.org/bj/436/bj4360341add.htm).

Mutagenesis of active-site histidine residues: kinetic parameters and pH profiles

In addition to the above tyrosine residue involved in substrate stabilization, the AAO active site also includes two conserved histidine residues (Figure 1). Using site-directed mutagenesis, we experimentally replaced these two histidine residues with serine and alanine residues in the H502S/A and H546S/A independent variants. The two H502S/A variants showed a strong turnover decrease (approximately 2900-fold), whereas the H546S/A mutations caused milder decreases (12- and 60-fold respectively) (Table 1). All of the substitutions also caused an increase in the K_m for the alcohol substrate, which was higher for the H502S/A (27- and 80-fold increases respectively) than for the H546S/A (8- and 25-fold increases respectively) variants. The above changes made the H546S, H546A, H502S and H502A

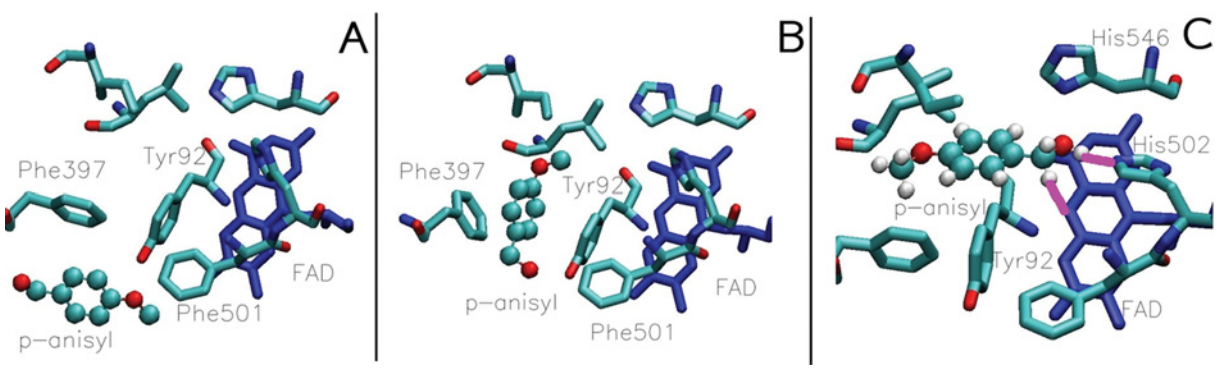

Figure 3 Three representative snapshots along substrate diffusion into the AAO active site

Three different situations during PELE-predicted migration of *p*-anisyl alcohol into the AAO active site are shown. (**C**) corresponds to a catalytically active conformation, where the proton- and hydride-transfer co-ordinates (to His[502] Nε and isoalloxazine N-5 respectively) are shown in pink. Alcohol entrance (**A**) and an intermediate position of the migration trajectory (**B**) are also shown.

Table 1 Steady- and transient-state kinetic parameters of wild-type recombinant AAO and its His^{502} and His^{546} variants in the reaction with *p*-anisyl alcohol as a substrate

Steady-state constants for native AAO and its H546S and H546A variants were determined by simultaneously varying the concentrations of *p*-anisyl alcohol and O_2 in 0.1 M phosphate (pH 6), at 25 °C, whereas those of the other variants were determined in air-saturated buffer (no O_2-concentration-dependence). Steady-state kinetic constants included turnover rates (k_{cat}) and Michaelis constants for the alcohol (K_m) measured at 25 °C. Transient-state kinetic constants included reduction (k_{red}) and dissociation (K_d) constants calculated at 12 °C and 25 °C for wild-type AAO and its variants respectively, using the buffer described above. ins, not determined because of H546S instability during stopped-flow determinations.

State	AAO	H502S	H502A	H546S	H546A
Steady-state					
k_{cat} (s^{-1})	208 ± 5	0.069 ± 0.005	0.072 ± 0.002	17 ± 1	3.5 ± 0.1
$K_{m(Al)}$ (μM)	48 ± 3	1289 ± 246	3820 ± 234	310 ± 56	1160 ± 33
k_{cat}/K_m ($mM^{-1} \cdot s^{-1}$)	4330 ± 290	0.054 ± 0.01	0.019 ± 0.001	53 ± 11	3.0 ± 0.1
Transient-state					
k_{red} (s^{-1})	139 ± 16	0.111 ± 0.002	0.076 ± 0.001	ins	3.96 ± 0.05
K_d (μM)	26 ± 5	4740 ± 184	3180 ± 74	ins	1310 ± 30

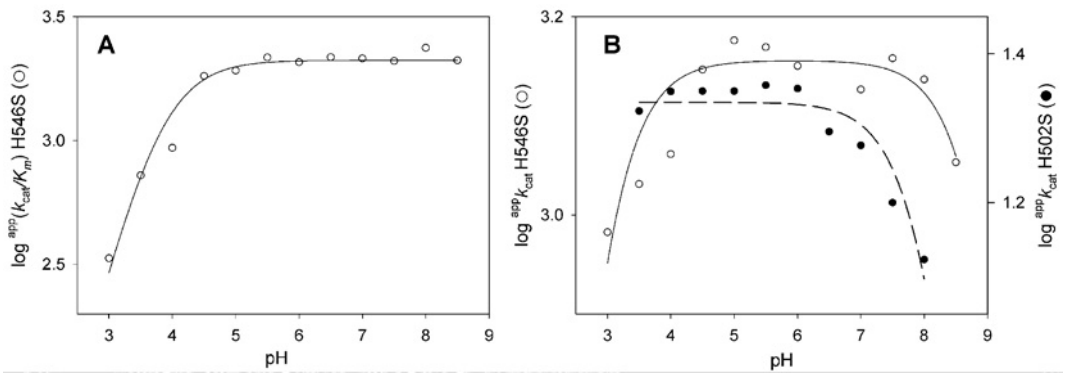

Figure 4 pH-dependence of kinetic constants for two mutated AAO variants

Apparent catalytic efficiency [$^{app}(k_{cat}/K_m)$ in $mM^{-1} \cdot min^{-1}$] (**A**) and turnover ($^{app}k_{cat}$ in min^{-1}) (**B**) for *p*-anisyl alcohol oxidation by the H546S and H502S AAO variants were determined at different pH values, under air saturation conditions at 25 °C, and presented using logarithmic transformation (and two different *y*-axes in **B**).

variants respectively, 80-, 1450-, 80 000- and over 200 000-fold less efficient than wild-type AAO in oxidizing *p*-anisyl alcohol.

The reductive (substrate oxidation) half-reactions of the H502S/A and H546A variants were further investigated under anaerobic conditions using stopped-flow spectrophotometry (the low stability of H546S prevented this characterization). As previously found for AAO, no intermediates were detected during flavin reduction to the hydroquinone state in these variants. The observed rate constants showed hyperbolic dependence on the *p*-anisyl alcohol concentration, allowing determination of AAO reduction (k_{red}) and substrate dissociation (K_d) constants (Table 1). The k_{red} values for the H546A, H502S, H502A and variants were at least 35-, 1200- and 1800-fold lower respectively than those of the wild-type AAO, and a strong decrease in the alcohol affinity (50–200-fold higher K_d values) was also observed. Taken together, these results confirm that both His^{502} and His^{546} participate in AAO catalysis, playing a crucial role during the reductive half-reaction.

Wild-type AAO does not show a clear pH-dependence for oxidation of *p*-anisyl alcohol and other alcohol substrates. However, replacement of His^{546} resulted in a clear effect of pH in the oxidation of *p*-anisyl alcohol (Figure 4). The catalytic efficiency profile of H546S showed a residue in the free enzyme with an apparent pK_a value of 3.8 that must be unprotonated for catalysis. The effect of pH on the variant turnover resulted in a bell-shaped profile, consistent with the involvement of two ionizable groups in the substrate-binding site. One group with a p$K_a \leqslant 3.5$ must be unprotonated for activity, and one with a p$K_a \geqslant 8.3$ must be protonated. As shown in Table 1, the activity of the H502S and H502A variants was extremely low, hampering catalytic efficiency estimation under different pH conditions. However, p$K_a \geqslant 7.5$ could be determined for the H502S turnover (Figure 4B). This corresponds to a residue that must be protonated during turnover at the same time that the previously observed p$K_a \leqslant 3.5$ disappeared, suggesting that it corresponds to the His^{502} removed in the present variant.

Protonation states of His^{502} and His^{546}, and other active-site residues

The mutational studies indicate the importance of His^{502} and His^{546} in catalysis, but do not reveal whether they are protonated at the δ/ε positions (Hid/Hie) or at both positions (Hip), a central aspect to identify the catalytic base. We have studied the protonation state of the Glu^{389}/His^{546}/His^{502}/His^{313} cluster with three different predictors. With the alcohol substrate present, all of these methods agreed that the net charge of the cluster should be zero, with the differences being which residue should be preferentially protonated. WHAT IF and ICDA show protonation of Glu^{389}, whereas APBS indicates protonation of His^{546}. Thus, as expected,

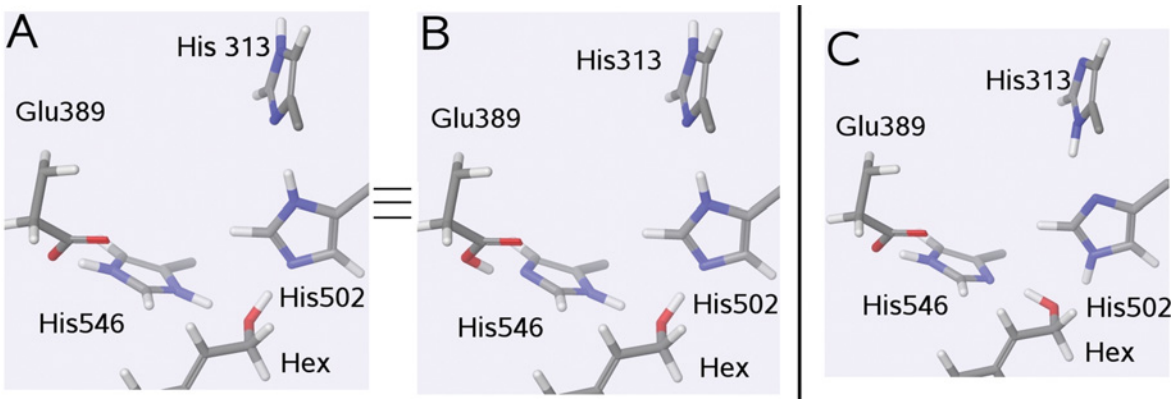

Figure 5 Putative protonation states of conserved histidine residues at the AAO active site

(**A**–**C**) The initial His^{546} protonation state (Hid^{502}/Hip^{546}, with His^{502} only protonated at Nδ and His^{546} doubly protonated) (**A**), the final His^{546} protonation state ($Glh^{389}/Hid^{502}/Hid^{546}$ or simply Glh^{389}/Hid^{502}, with both histidine residues only being protonated at Nδ and Glu^{389} being protonated) (**B**), and the His^{502} protonation state (Hie^{502}/Hie^{546}, with both histidine residues only being protonated at Nε) (**C**). The side chain of His^{546} has been flipped with respect to the deposited crystal structure.

the negative charge of Glu^{389} in the active site is screened, although it is not clear which residue carries the proton.

To determine more accurately which of these would be protonated, a QM/MM minimization was performed on the substrate-free crystal structure with the three histidine residues, the glutamic acid residue and the flavin included as the QM region. When His^{546} was protonated (Hip^{546}), a spontaneous proton transfer occurred between His^{546} and Glu^{389}, forming a neutral glutamic acid residue, Glh^{389}, and reducing the charge separation in the active site. When His^{313} or His^{502} were protonated (to give Hip^{313} or Hip^{502}), this resulted in a less stable conformation ($+8.9$ and $+2.5$ kcal $\cdot$ mol^{-1} respectively) than His^{546} being protonated. The heavy-atom RMSD (root mean square deviation) to the crystal structure was also smaller when Hip^{546} was protonated (0.63 Å) confirming that the final state, with the neutral Glu^{389}, is the correct starting configuration. The same results were obtained with *p*-anisyl alcohol bound. The neutral nature of Glu^{389} agrees with its buried hydrophobic environment in the crystal structure. This is in contrast with the equivalent glutamic acid residue in CHO, Glu^{312}, which is in contact with a large water cluster in the crystal structure. APBS, for example, gives a pK_a for Glu^{389} of 8.19 (similar to the highest pK_a experimentally obtained for the AAO histidine variants; Figure 4B) corresponding to a residue that should be protonated for catalysis, whereas we obtain a value of 5.4 for Glu^{312} in CHO.

To further explore the possible combinations between His^{502} and His^{546}, we performed 5 ns MD for six different protonation states: His^{546} in three possible protonation states (Hid, Hie and Hip) times two possible protonation states for His^{502} (Hid and Hie). The results show that only the combination of Hip^{546} and Hid^{502} produced a stable catalytic species where both the proton abstraction (by the histidine base) and the hydride transfer (to flavin N-5) distances were simultaneously optimal (see the Supplementary Results section and Supplementary Figure S2 at http://www.BiochemJ.org/bj/436/bj4360341add.htm). To illustrate the situation, Figures 5(A) and 5(B) indicate the initial and final states when His^{546} is protonated, which is favoured by the QM/MM and MD simulations, and Figure 5(C) indicates the Hie^{502}/Hie^{546} protonation state.

QM/MM analysis of the AAO and CHO enzymatic reactions

From the catalytically active species produced after ligand migration, we proceeded to compute the QM/MM energy profile for the alcohol oxidation. Previous analyses have indicated that the $Glh^{389}/Hid^{502}/Hid^{546}$ state is preferred to the Hie^{502}/Hie^{546} one (Figures 5B and 5C respectively). We have built, however, the oxidation energy profiles for both cases, which were labelled as Glh^{389}/Hid^{502} and Hie^{502}/Hie^{546}. In the first case, His^{502} accepts the proton and His^{546} hydrogen-bonds the oxygen alcohol. For the Hie^{502}/Hie^{546} case the roles are inverted.

Figure 6(A) shows the energy profile obtained for these two protonation states for *p*-anisyl alcohol. As expected in these types of reaction mechanism, the profiles indicate that the proton is the first to be transferred; starting the process with the hydride results in larger (and earlier) energy barriers. In all cases, the main component of the energy barrier corresponds to the hydride transfer. Figure 6(B) shows the corresponding energy profiles for the 2,4-hexadien-1-ol oxidation. We plot the energy profiles where the proton is being transferred first since the hydride first mechanism gave identical results as in the *p*-anisyl case. The third mechanism explored, the concerted-synchronous transfer with simultaneous transfer of the proton and hydride, introduces higher barriers for both substrates. All attempts to locate a transition state for the synchronous transfer, in any of the substrates, resulted in barriers above 30 kcal $\cdot$ mol^{-1}.

In the Hie^{502}/Hie^{546} case (Figure 5C), transferring the proton to Hie^{546} involves a second spontaneous proton-transfer event to Glu^{389} in both 2,4-hexadien-1-ol and *p*-anisyl alcohol. Therefore the glutamic acid side chain acts as the final base, in agreement with the previous protonation and pK_a calculations. In the Glh^{389}/Hid^{502} case (Figure 5B), His^{502} is hydrogen-bonded to another histidine residue, His^{313}, which could act as the final base. However, all attempts to expand the proton relay to His^{313}, before and after the hydride transfer and for both substrates, resulted in non-stable structures, the proton being transferred back to His^{502}.

The crystal structure in CHO indicates a correlation between His^{466} and AAO His^{502}, whereas the position of AAO His^{546} is occupied by an asparagine residue in CHO (Figure 1). There is, however, a second histidine residue in CHO capable of acting as a base: His^{351}. We have tried four different possibilities for the base in CHO using QM/MM: His^{351}, His^{466}, Glu^{312} and the flavin O-4. Only when using His^{466} as a base did we obtain a low barrier energy profile with a stable alkoxide intermediate. Using flavin O-4 as a base results in a profile with an ~40 kcal energy increase. Analogous to His^{546} in AAO, abstraction of a proton from His^{351} induced a spontaneous transfer from the

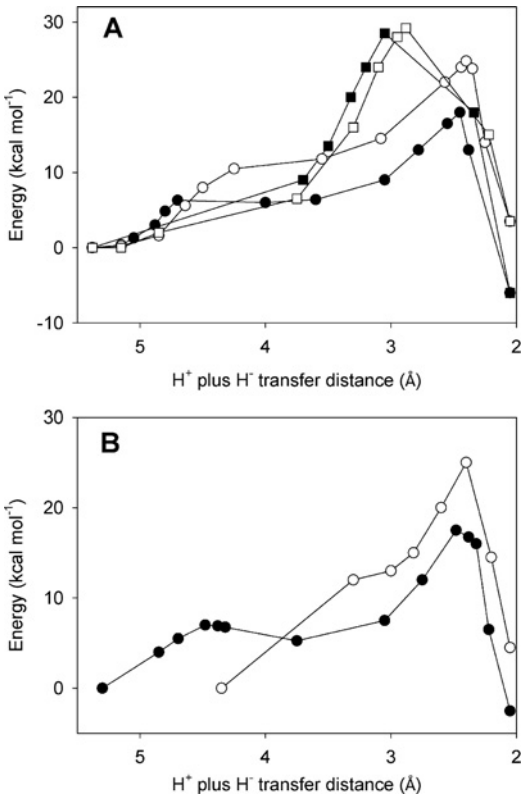

Figure 6 Reaction profiles of *p*-anisyl alcohol and 2,4-hexadien-1-ol dehydrogenation by AAO

QM/MM energy profiles obtained for the reactions of AAO with *p*-anisyl alcohol (**A**) and 2,4-hexadien-1-ol (**B**). In these computations, two protonation states of Glu^{389}, His^{502} and His^{546} (Figures 5B and 5C), and two orders or the hydride+proton-transfer reaction were considered in the following combinations: (i) $Glh^{389}/Hid^{502}/Hid^{546}$ state and reaction initiated by proton transfer (○); (ii) $Glh^{389}/Hid^{502}/Hid^{546}$ and reaction initiated by hydride transfer (□); (iii) Hie^{502}/Hie^{546} state and reaction initiated by proton transfer (●); and (iv) Hie^{502}/Hie^{546} state and reaction initiated by hydride transfer (■). The course of the reaction, from left to right on the *x*-axis, was estimated as the total distance between the alcohol hydroxy hydrogen and the catalytic histidine residue (H^+ transfer), plus the distance between its benzylic hydrogen and the flavin N-5 (H^- transfer).

histidine residue to Glu^{312}. Thus the final state is the same when using His^{351} or Glu^{312} as a base. The energy profile indicates a barrier of ~20 kcal · mol^{-1} and endothermicity of 18 kcal · mol^{-1}, which translates into a non-stable alkoxide intermediate.

Figure 7 compares the CHO and AAO energy profiles when using His^{466} and His^{502} respectively as bases. CHO oxidation presents a low energy barrier, ~10 kcal · mol^{-1}, and has a stable intermediate as a result of the first proton-transfer event, ~6 kcal · mol^{-1} higher than the reactants, whereas no intermediate was stabilized in the AAO reaction. Moreover, in contrast with that observed in AAO, the alcohol proton abstraction in CHO drives a second spontaneous proton transfer from His^{466} to His^{310} (Figure 1). The second proton transfer results in ~3 kcal · mol^{-1} relaxation, being a significant part of the intermediate stabilization in CHO. As seen in Figure 7, the energy profile for the second part of the process, the hydride transfer, is almost identical in both systems; the exothermicity of the process in CHO comes mainly from the intermediate stabilization.

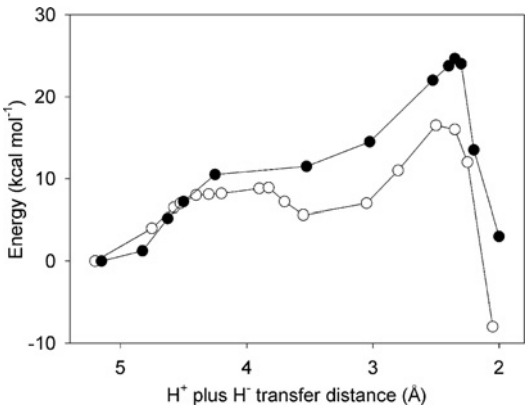

Figure 7 Energy profiles for *p*-anisyl alcohol oxidation by AAO and choline oxidation by CHO

The energy profiles for *p*-anisyl alcohol oxidation by AAO (●) and choline oxidation by CHO (○), in reactions initiated by proton transfer to the catalytic base (His^{502} and His^{466} respectively) followed by hydride transfer to flavin N-5, were obtained by QM/MM calculations. The course of the reaction, from left to right on the *x*-axis, was estimated as the total distance between the alcohol hydroxy hydrogen and the catalytic histidine (H^+ transfer), plus the distance between its benzylic hydrogen and the flavin N-5 (H^- transfer).

DISCUSSION

Substrate diffusion to reach the buried active site of AAO

The simulations on ligand binding and migration clearly indicate that the alcohol substrate entrance into the active site of AAO is highly coupled to oscillations of the Gln^{395}–Thr^{406} loop. As recently reported [7], this loop represents a characteristic structural feature of AAO crystal structure, when compared with glucose oxidase and CHO structures. Although its active-site entrance is considerably more open, owing to the absence of the loop, a gating mechanism has recently been proposed in CHO [30].

The energy profile shows the existence of an intermediate along the PELE migration pathway, where the AAO ligand interacts with Phe^{397}. Ligand entrance coupled to phenylalanine motions seems to be a common feature and has been observed in several systems, such as cytochrome P450cam [14,31]. Once in the active site, the ligand easily adopts a catalytic position, with the alcohol hydrogen pointing to the possible histidine bases, and one of the α-hydrogens pointing to the FAD N-5 for hydride transfer (at 2.4–2.5 Å distances) by means of a π–π interaction with Tyr^{92}. The present study suggests that the latter is a T-shaped interaction. T-shaped stacking interactions have been largely characterized in biological systems [32], also being one of the main local minima in the benzene dimer [33]. Reported mutations of AAO Tyr^{92} [6] have shown that an aromatic residue is required at this position, the Y92A variant being inactive but the Y92F variant maintaining basically the same kinetic parameters of the wild-type enzyme, supporting the involvement of the above π–π interaction in AAO catalysis.

Concerted non-synchronous mechanism for alcohol oxidation by AAO

The role of conserved active-site histidine residues as putative catalytic bases and acids for the reductive and oxidative half-reactions respectively has been extensively discussed in the GMC superfamily [8,34–36].

Our mutational studies indicate the importance of the two AAO histidine residues in the first step of the redox process (i.e. the reductive half-reaction). His^{546} seems to play a similar role in substrate binding and oxidation, as revealed by a 20–60-fold decrease in k_{cat} and k_{red}, and similar increases in alcohol K_m and K_d, for the H546A variant. This role of His^{546} on substrate stabilization agrees with the MM studies. The Hid^{502}/Hip^{546} protonation state produces the best alignment for the ligand catalysis, with an optimal proton- and hydride-transfer distance. Inspection of the crystal structure, with His^{546} lying next to Glu^{389}, seems to indicate the positive nature of the former residue (or the protonation of Glu^{389}). The protonation studies further agree with this visual inspection: Glu^{389} is protonated, with His^{546} and His^{502} being neutral and with δ protonation. Thus, in the wild-type enzyme, we would expect His^{502} to act as the base, in agreement with the mutational studies showing an approximate 3000-fold decrease in k_{cat}, and at least a 1000-fold decrease in k_{red}, after its substitution by alanine or serine. It is necessary to mention that, in addition to its main role as the catalytic base, an effect on substrate binding is also exerted by His^{502}, resulting in lower affinity (27–80-fold higher alcohol K_m, and 100–200-fold higher K_d) in the above variants. Mutations that might open the AAO active site or change its polarization, decreasing Glu^{389} pK_a, would open the possibility of using His^{546} as a base.

The AAO QM/MM energy profiles indicate the presence of very weak (with a $\sim$1–2 kcal $\cdot$ mol^{-1} barrier back to the reactants) intermediates in alcohol oxidation. The calculations provide only internal energies, not including vibration zero-point nor thermal energies. Corrections for these energies are in the order of 3–4 kcal $\cdot$ mol^{-1} for a proton-transfer reaction [37–39] (see, for example, Figure 3 in [37]). Thus including these effects in all energy profiles will present no intermediates, indicating a concerted mechanism for the proton and hydride transfers in AAO catalysis. This is in agreement with mechanistic studies using α-dideuterated *p*-anisyl alcohol and 2,4-hexadien-1-ol as substrates and deuterium oxide as reaction solvent [40]. The former revealed a strong substrate kinetic effect, and supported the hydride-transfer mechanism in AAO, whereas the latter showed the existence of a low, but consistent, solvent KIE (and clear multiple KIEs when both deuterated substrate and solvent were combined) for AAO oxidation of alcohol substrates (Table 2). These KIEs were observed under both steady-state and transient-state conditions, and were indicative of a concerted proton- and hydride-transfer mechanism. A similar concerted proton- and hydride-transfer mechanism has recently been reported for AAO oxidation of some aromatic aldehydes bearing electron-withdrawing substituents, which promote formation of the *gem*-diol substrates [41]. A concerted mechanism occurs in a single step, but it does not tell anything of the synchronous or non-synchronous bond breaking. We have investigated both mechanisms for alcohol oxidation by AAO, and any attempt to locate a synchronous proton and hydride transfer resulted in very large barriers, whereas the non-synchronous mechanism was significantly lower in energy. Non-synchronous concerted oxidation mechanisms, as described here for AAO, have been reported for other oxidoreductases [42].

Table 2 Comparison of substrate, solvent and multiple KIEs

The KIEs on the apparent k_{cat} and the k_{red} constants for AAO oxidation of α-dideuterated *p*-anisyl alcohol and 2,4-hexadien-1-ol, and CHO oxidation of 1,2-tetradeuterated choline are shown. The substrate KIE (^{2H}k) is the ratio between the activity on the non-deuterated and the deuterated substrate; the solvent KIE ($^{2H_2O}k$) is the ratio between the activity in H_2O and ^2H_2O, and the multiple KIE ($^{2H,^2H_2O}k$) is the ratio between the activity on the non-deuterated substrate in water and the deuterated substrate in ^2H_2O.

	AAO*		CHO†
KIE	*p*-anisyl alcohol	2,4-hexadien-1-ol	choline
$^{2H}k_{cat}$	5.4 $\pm$ 0.1	5.6 $\pm$ 0.1	7.3 $\pm$ 1.0
$^{2H}k_{red}$	9.0 $\pm$ 0.8	8.9 $\pm$ 0.2	8.9 $\pm$ 0.2
$^{2H_2O}k_{cat}$	1.35 $\pm$ 0.06	1.25 $\pm$ 0.03	1.1$\pm$0.1
$^{2H^2H_2O}k_{cat}$	7.0 $\pm$ 0.4	7.0 $\pm$ 0.2	7.3 $\pm$ 0.2
$^{2H_2O}k_{red}$	1.42 $\pm$ 0.10	1.33 $\pm$ 0.02	0.99 $\pm$ 0.02
$^{2H^2H_2O}k_{red}$	13.5 $\pm$ 0.9	12.5 $\pm$ 0.3	8.4 $\pm$ 0.2

*From Ferreira et al. [40].
†From Fan and Gadda [43].

Catalytic mechanisms in GMC oxidoreductases: a comparison between CHO and AAO

The catalytic mechanism of CHO has been investigated in detail as a model GMC oxidoreductase [8]. In CHO the active-site polarity changes significantly with respect to AAO. The pK_a analysis of its active-site glutamic acid residue, Glu^{312}, reveals an anionic side chain at physiological pH. Mutation of Glu^{312} causes a 500-fold increase in the K_d value [11]. Thus it seems clear that this glutamic acid residue remains negative for an effective interaction with the trimethylammonium group of choline.

When comparing the CHO QM/MM energy profiles, we obtain His^{466} as the main base (in both AAO and CHO the histidine residue in front of the flavin appears as the base). The reduction in pK_a for Glu^{312}, compared with that for Glu^{389} in AAO, drastically increases the energy barrier and intermediate energies for the second histidine path in CHO, the His^{351}–Glu^{312} path. Although the studies of Gadda and co-workers [10,12] have not definitively concluded the nature of the CHO base, mutation of His^{466} has the larger effect on k_{cat}. More recently, Gadda [8] suggested that either one of the active-site histidine residues in CHO (His^{351} and His^{466}) act as the base (being replaced by the second histidine residue when mutated) or, alternatively, the acidification of the substrate hydroxy group and proton loss to the solvent may occur through interactions with multiple active-site residues. However, the observation of a two-step kinetic process in CHO, and the existence of a stable intermediate in the QM/MM energy profiles obtained in the present study, suggest His^{466} as being the base in CHO. H466A mutation drastically reduces k_{cat} and eliminates the two-step process [8,10], which would be consistent with the activation of the His^{351}–Glu^{312} path, with a proton abstraction energy barrier equivalent to that of the hydride transfer.

One of the main differences between CHO and AAO is the presence of a stable intermediate for the initial proton transfer in CHO. This intermediate is partially the result of a proton relay involving His^{466} and His^{310}. The same mechanism could be operative in AAO owing to the presence of His^{313}. However, our calculations indicate that in AAO this second proton transfer does not occur. The local environment of this second histidine residue is significantly different in both enzymes. In CHO, His^{310} is in closer interaction with two carbonyl groups, from Val^{507} and Thr^{380}, and its side chain forms a stacking interaction with another histidine side chain, that of His^{506}. Thus the proton relay in CHO seems more favourable owing to the electrostatic stabilization of the two carbonyl groups and the π-cation interaction with His^{506}. The existence of a stable intermediate in the proton transfer in CHO agrees with the observations of a two-step process for this enzyme, as opposed to the concerted mechanism observed in AAO. The existence of these divergent mechanisms is in agreement with the absence of a solvent KIE in choline oxidation by CHO investigated

under both steady-state and transient-state conditions [43,44], whereas a solvent effect was observed for AAO oxidation of the two alcohols investigated in the present study [40] (Table 2). The non-synchronous concerted mechanism for alcohol oxidation by AAO, on the basis of both the KIE results and QM/MM energy profiles, would be different from the sequential mechanism proposed for CHO and other GMC oxidoreductases [8,43].

Conclusions

Using experimental and computational techniques we have studied the ligand diffusion and oxidation processes in AAO, compared with CHO. We find that the substrate entrance is next to the Gln^{395}–Thr^{406} loop, bypassing and interacting with Phe^{397} and, once in the active site, side-chain readjustment is required for a stacking interaction with Tyr^{92}. QM/MM and site-directed mutagenesis results show that His^{502} and His^{546} are involved in catalysis, their substitution strongly decreasing both k_{cat} and k_{red}. The theoretical energy profiles, protonation predictors and mutagenesis studies provide a robust answer regarding the nature of the catalytic base: the histidine residue directly in front of the FAD cofactor ring (AAO His^{502}, corresponding to CHO His^{466}) acts as the base. Furthermore, for the two substrates assayed, it was shown that proton transfer preceded hydride transfer, although both processes are highly coupled. In AAO the QM/MM energies do not find a stable intermediate along the proton- and hydride-transfer co-ordinates. In CHO, however, we find a stable intermediate after proton abstraction, in agreement with previous findings. The atomic resolution of the computational analysis allows us to narrow down these differences with changes in the active site. Overall the combination of theoretical and solvent KIE studies suggests a non-synchronous concerted mechanism for alcohol oxidation by AAO.

AUTHOR CONTRIBUTION

Aitor Hernández-Ortega, Patricia Ferreira, Milagros Medina and Angel Martínez contributed to the experimental part of the work, and Kenneth Borrelli and Victor Guallar contributed to the computational part of the work. Although all of the authors participated in the interpretation and discussion of results, Victor Guallar, Angel Martínez and Milagros Medina especially contributed to integrate the two parts of the study.

ACKNOWLEDGEMENTS

We thank the Barcelona Supercomputing Center for computational resources.

FUNDING

This work was supported by the Spanish Ministries of Education and Science [grant number CTQ2007-62122 (to V.G.)]; the Spanish Ministries of Science and Innovation [grant numbers BIO2010-1493 (to M.M.) and BIO2008-01533 (to A.T.M.)]; and by the European Union [grant numbers NMP2-CT-2006-026456 (BIORENEW) and KBBE-2010-4-265397 (PEROXICATS) (to A.T.M.)]. A.H.-O. thanks a predoctoral contract from the Comunidad de Madrid, and P.F. thanks a Juan de la Cierva contract of the Spanish Ministry of Science and Innovation.

REFERENCES

1 Ferreira, P., Medina, M., Guillén, F., Martínez, M. J., van Berkel, W. J. H. and Martínez, A. T. (2005) Spectral and catalytic properties of aryl-alcohol oxidase, a fungal flavoenzyme acting on polyunsaturated alcohols. Biochem. J. **389**, 731–738
2 Ruiz-Dueñas, F. J. and Martínez, A. T. (2009) Microbial degradation of lignin: how a bulky recalcitrant polymer is efficiently recycled in nature and how we can take advantage of this. Microbiol. Biotechnol. **2**, 164–177
3 Martínez, A. T., Ruiz-Dueñas, F. J., Martínez, M. J., del Río, J. C. and Gutiérrez, A. (2009) Enzymatic delignification of plant cell wall: from nature to mill. Curr. Opin. Biotechnol. **20**, 348–357
4 Varela, E., Martínez, A. T. and Martínez, M. J. (1999) Molecular cloning of aryl-alcohol oxidase from *Pleurotus eryngii*, an enzyme involved in lignin degradation. Biochem. J. **341**, 113–117
5 Varela, E., Martínez, M. J. and Martínez, A. T. (2000) Aryl-alcohol oxidase protein sequence: a comparison with glucose oxidase and other FAD oxidoreductases. Biochim. Biophys. Acta **1481**, 202–208
6 Ferreira, P., Ruiz-Dueñas, F. J., Martínez, M. J., van Berkel, W. J. H. and Martínez, A. T. (2006) Site-directed mutagenesis of selected residues at the active site of aryl-alcohol oxidase, an H_2O_2-producing enzyme. FEBS J. **273**, 4878–4888
7 Fernández, I. S., Ruiz-Dueñas, F. J., Santillana, E., Ferreira, P., Martínez, M. J., Martínez, A. T. and Romero, A. (2009) Novel structural features in the GMC family of oxidoreductases revealed by the crystal structure of fungal aryl-alcohol oxidase. Acta Crystallogr. Sect. D Biol. Crystallogr. **65**, 1196–1205
8 Gadda, G. (2008) Hydride transfer made easy in the reaction of alcohol oxidation catalyzed by flavin-dependent oxidases. Biochemistry **47**, 13745–13753
9 Menon, V., Hsieh, C. T. and Fitzpatrick, P. F. (1995) Substituted alcohols as mechanistic probes of alcohol oxidase. Bioorg. Chem. **23**, 42–53
10 Ghanem, M. and Gadda, G. (2005) On the catalytic role of the conserved active site residue His466 of choline oxidase. Biochemistry **44**, 893–904
11 Quaye, O., Lountos, G. T., Fan, F., Orville, A. M. and Gadda, G. (2008) Role of Glu312 in binding and positioning of the substrate for the hydride transfer reaction in choline oxidase. Biochemistry **47**, 243–256
12 Rungsrisuriyachai, K. and Gadda, G. (2008) On the role of histidine 351 in the reaction of alcohol oxidation catalyzed by choline oxidase. Biochemistry **47**, 6762–6769
13 Gutiérrez, A., Caramelo, L., Prieto, A., Martínez, M. J. and Martínez, A. T. (1994) Anisaldehyde production and aryl-alcohol oxidase and dehydrogenase activities in ligninolytic fungi from the genus *Pleurotus*. Appl. Environ. Microbiol. **60**, 1783–1788
14 Borrelli, K. W., Vitalis, A., Alcantara, R. and Guallar, V. (2005) PELE: protein energy landscape exploration. A novel Monte Carlo based technique. J. Chem. Theory Comput. **1**, 1304–1311
15 Senn, H. M. and Thiel, W. (2007) QM/MM methods for biological systems. Top. Curr. Chem. **268**, 173–290
16 Friesner, R. A. and Guallar, V. (2005) *Ab initio* quantum chemical and mixed quantum mechanics/molecular mechanics (QM/MM) methods for studying enzymatic catalysis. Annu. Rev. Phys. Chem. **56**, 389–427
17 Ruiz-Dueñas, F. J., Ferreira, P., Martínez, M. J. and Martínez, A. T. (2006) *In vitro* activation, purification, and characterization of *Escherichia coli* expressed aryl-alcohol oxidase, a unique H_2O_2-producing enzyme. Protein Expression Purif. **45**, 191–199
18 Fraaije, M. W. and van Berkel, W. J. H. (1997) Catalytic mechanisms of the oxidative demethoxylation of 4-(methoxymethyl)phenol by vanillyl-alcohol oxidase. Evidence for formation of a *p*-quinone methide intermediate. J. Biol. Chem. **272**, 18111–18116
19 Jacobson, M. P., Pincus, D. L., Rapp, C. S., Day, T. J. F., Honig, B., Shaw, D. E. and Friesner, R. A. (2004) A hierarchical approach to all-atom protein loop prediction. Proteins **55**, 351–367
20 Orville, A. M., Lountos, G. T., Finnegan, S., Gadda, G. and Prabhakar, R. (2009) Crystallographic, spectroscopic, and computational analysis of a flavin C4a-oxygen adduct in choline oxidase. Biochemistry **48**, 720–728
21 Guallar, V., Lu, C. Y., Borrelli, K., Egawa, T. Y. and Yeh, S. R. (2009) Ligand migration in the truncated hemoglobin-II from *Mycobacterium tuberculosis*: the role of G8 tryptophan. J. Biol. Chem. **284**, 3106–3116
22 Borrelli, K., Cossins, B. and Guallar, V. (2010) Exploring hierarchical refinement techniques for induced fit docking with protein and ligand flexibility. J. Comp. Chem. **31**, 1224–1235
23 Halgren, T. (2007) New method for fast and accurate binding-site identification and analysis. Chem. Biol. Drug Design **69**, 146–148
24 Vriend, G. (1990) WHAT IF: a molecular modeling and drug design program. J. Mol. Graphics **8**, 52–56
25 Baker, N. A., Sept, D., Joseph, S., Holst, M. J. and McCammon, J. A. (2001) Electrostatics of nanosystems: application to microtubules and the ribosome. Proc. Natl. Acad. Sci. U.S.A. **98**, 10037–10041
26 Li, X., Jacobson, M. P., Zhu, K., Zhao, S. and Friesner, R. A. (2007) Assignment of polar states for protein amino acid residues using an interaction cluster decomposition algorithm and its application to high resolution protein structure modeling. Proteins **66**, 824–837
27 Phillips, J. C., Braun, R., Wang, W., Gumbart, J., Tajkhorshid, E., Villa, E., Chipot, C., Skeel, R. D., Kale, L. and Schulten, K. (2005) Scalable molecular dynamics with NAMD. J. Comp. Chem. **26**, 1781–1802
28 Reference deleted

29 Reference deleted
30 Xin, Y., Gadda, G. and Hamelberg, D. (2009) The cluster of hydrophobic residues controls the entrance to the active site of choline oxidase. Biochemistry **48**, 9599–9605
31 Fishelovitch, D., Shaik, S., Wolfson, H. J. and Nussinov, R. (2009) Theoretical characterization of substrate access/exit channels in the human cytochrome P450 3A4 enzyme: involvement of phenylalanine residues in the gating mechanism. J. Phys. Chem. B **113**, 13018–13025
32 Meyer, E. A., Castellano, R. K. and Diederich, F. (2003) Interactions with aromatic rings in chemical and biological recognition. Angew. Chem. Int. Ed. **42**, 1210–1250
33 Dinadayalane, T. C. and Leszczynski, J. (2009) Geometries and stabilities of various configurations of benzene dimer: details of novel V-shaped structure revealed. Struct. Chem. **20**, 11–20
34 Roth, J. P. and Klinman, J. P. (2003) Catalysis of electron transfer during activation of O_2 by the flavoprotein glucose oxidase. Proc. Natl. Acad. Sci. U.S.A. **100**, 62–67
35 Su, Q. and Klinman, J. P. (1999) Nature of oxygen activation in glucose oxidase from *Aspergillus niger*: the importance of electrostatic stabilization in superoxide formation. Biochemistry **38**, 8572–8581
36 Wohlfahrt, G., Witt, S., Hendle, J., Schomburg, D., Kalisz, H. M. and Hecht, H.-J. (1999) 1.8 and 1.9 Å resolution structures of the *Penicillium amagasakiense* and *Aspergillus niger* glucose oxidase as a basis for modelling substrate complexes. Acta Crystallogr. Sect. D Biol. Crystallogr. **55**, 969–977
37 Agarwal, P. K., Billeter, S. R. and Hammes-Schiffer, S. (2002) Nuclear quantum effects and enzyme dynamics in dihydrofolate reductase catalysis. J. Phys. Chem. B **106**, 3283–3293
38 Guallar, V., Harris, D. L., Batista, V. S. and Miller, W. H. (2002) Proton-transfer dynamics in the activation of cytochrome P450eryF. J. Am. Chem. Soc. **124**, 1430–1437
39 Truong, T. N. and McCammon, J. A. (1991) Direct dynamics study of intramolecular proton-transfer in hydrogenoxalate anion. J. Am. Chem. Soc. **113**, 7504–7508
40 Ferreira, P., Hernández-Ortega, A., Herguedas, B., Martínez, A. T. and Medina, M. (2009) Aryl-alcohol oxidase involved in lignin degradation: a mechanistic study based on steady and pre-steady state kinetics and primary and solvent isotope effects with two different alcohol substrates. J. Biol. Chem. **284**, 2480–2487
41 Ferreira, P., Hernández-Ortega, A., Herguedas, B., Rencoret, J., Gutiérrez, A., Martínez, M. J., Jiménez-Barbero, J., Medina, M. and Martínez, A. T. (2010) Kinetic and chemical characterization of aldehyde oxidation by fungal aryl-alcohol oxidase. Biochem. J. **425**, 585–593
42 Newcomb, M., Letadicbiadatti, F. H., Chestney, D. L., Roberts, E. S. and Hollenberg, P. F. (1995) A nonsynchronous concerted mechanism for cytochrome-P-450 catalyzed hydroxylation. J. Am. Chem. Soc. **117**, 12085–12091
43 Fan, F. and Gadda, G. (2005) On the catalytic mechanism of choline oxidase. J. Am. Chem. Soc. **127**, 2067–2074
44 Gadda, G. (2003) pH and deuterium kinetic isotope effects studies on the oxidation of choline to betaine-aldehyde catalyzed by choline oxidase. Biochim. Biophys. Acta **1650**, 4–9

Received 14 December 2010/16 February 2011; accepted 4 March 2011
Published as BJ Immediate Publication 4 March 2011, doi:10.1042/BJ20102090

Biochem. J. (2011) **436**, 341–350 (Printed in Great Britain) doi:10.1042/BJ20102090

multimedia online data

SUPPLEMENTARY ONLINE DATA

Substrate diffusion and oxidation in GMC oxidoreductases: an experimental and computational study on fungal aryl-alcohol oxidase

Aitor HERNÁNDEZ-ORTEGA*[1], Kenneth BORRELLI†[1], Patricia FERREIRA‡, Milagros MEDINA‡, Angel T. MARTÍNEZ*[2] and Victor GUALLAR†[2]

*Centro de Investigaciones Biológicas, Consejo Superior de Investigaciones Científicas (CSIC), Ramiro de Maeztu 9, E-28040 Madrid, Spain, †Catalan Institution for Research and Advanced Studies, Barcelona Supercomputing Center, Edificio Nexus II, E-08028 Barcelona, Spain, and ‡Department of Biochemistry and Molecular and Cellular Biology and Institute of Biocomputation and Physics of Complex Systems, University of Zaragoza, E-50009 Zaragoza, Spain

EXPERIMENTAL

Site-directed mutagenesis oligonucleotides

For site-directed mutagenesis using PCR, the following oligonucleotides (direct sequences) bearing mutations (underlined) at the corresponding triplets (bold) were used as primers: (i) H502S, 5′-GCCAACACGATTTTC**AG**CCCAGTTGGAACGGCC-3′; (ii) H502A, 5′-GCCAACACGATTTTC**GC**CCCAGTTGGAACGGCC-3′; (iii) H546S, 5′-CCCTTCGCGCCCAACGCA**AGT**ACCCAAGGACCG-3′; and (iv) H546A, 5′-CCCTTCGCGCCCAACGCA**GCT**ACCCAAGGACCG-3′.

Steady-state kinetic constants

Steady-state kinetic constants for the wild-type AAO, and the H546S and H546A variants were determined varying simultaneously the concentration of *p*-anisyl alcohol (4–2000 μM) and O_2 (51, 128, 273, 566 and 1279 μM) in 0.1 M phosphate (pH 6), at 25 °C. The constants were obtained by fitting (using Sigmaplot) the initial rate data to eqn (1) which describes a ternary complex mechanism with intersecting lines in double reciprocal plots, where e represents the enzyme concentration; k_{cat} is the maximal turnover; A is the concentration of alcohol; B is the concentration of O_2; K_{Am} and K_{Bm} are the Michaelis constants for A and B respectively; and K_{Ai} is the dissociation constant for A.

$$\frac{v}{e} = \frac{k_{cat} AB}{K_{Bm}A + K_{Am}B + AB + K_{Ai}K_{Bm}} \quad (1)$$

Steady-state kinetic constants for the H502S and H502A variants were determined by varying the alcohol concentration (62–5000 μM) under air-saturated buffer, since the (low) enzyme turnover rates were independent from O_2 concentration. The constants were obtained by fitting the initial rate data to the Michaelis–Menten equation.

pH-dependence profiles

The pH-dependence of the apparent catalytic constant, $^{app}k_{cat}$, and efficiency, $^{app}(k_{cat}/K_m)$, was determined by fitting initial rates to eqn (2–4). Data showing a slope of +1 and −1 were fitted to eqn 2 and eqn 3, where pK_{a1} and pK_{a2} represent the pK_a values of the acid and basic residues respectively. Data for the bell-shaped pH rate profile were fitted to eqn 4. C is the pH-independent value of the kinetic parameter of interest.

$$\log Y = \log\left(\frac{C}{1 + \frac{10^{-pH}}{10^{-pK_{a1}}}}\right) \quad (2)$$

$$\log Y = \log\left(\frac{C}{1 + \frac{10^{-pK_{a2}}}{10^{-pH}}}\right) \quad (3)$$

$$\log Y = \log\left(\frac{C}{1 + \frac{10^{-pH}}{10^{-pK_{a1}}} + \frac{10^{-pK_{a2}}}{10^{-pH}}}\right) \quad (4)$$

Stopped-flow kinetic measurements

An Applied Photophysics SX18.MV stopped-flow spectrophotometer, interfaced with an Acorn computer, was used. The SX18.MV and Xscan software were applied to experiments with single-wavelength and diode-array (350–700 nm) detectors respectively. Reductive half-reactions were studied under anaerobic conditions. Tonometers containing enzyme or substrate solutions were made anaerobic by successive evacuation and flushing with argon. These solutions also contained glucose (10 mM) and glucose oxidase (10 units · ml^{-1}) to ensure anaerobic conditions. Drive syringes in the apparatus were made anaerobic by sequentially passing dithionite and O_2-free buffer.

Measurements were carried out in 0.1 M phosphate buffer (pH 6), at 25 °C for H502S, H502A and H546A variants, and at 12 °C for wild-type AAO due to its extremely rapid reduction. Spectral evolution analysis of reductive-half reactions was performed by global analysis and numerical integration methods using the Pro-K software (Applied Photophysics). Data were fitted to a single-step A→B model where species A and B are the spectral species of oxidized and reduced enzyme respectively. Accurate observed rate constants (k_{obs}) were obtained from single-wavelength traces at 463 nm (wild-type AAO) or 468 nm (H502S, H502A and H546A variants), and fitted using a standard single exponential decay. k_{obs} values at different substrate concentrations (S) were fitted to eqn (5), where k_{red} and K_d are the flavin reduction and dissociation constants respectively.

$$k_{obs} = \frac{k_{red}S}{K_d + S} \quad (5)$$

[1] These authors contributed equally to this work.
[2] Correspondence may be addressed to either of these authors (email atmartinez@cib.csic.es or victor.guallar@bsc.es).

RESULTS

Hydrogen-bond network MD

To further explore the possible combinations between His^{502} and His^{546}, we performed 5 ns MD for six different protonation states: His^{546} in three possible protonation states (Hid, Hie and Hip) times two possible protonation states for His^{502} (Hid and Hie). The protonation state of His^{313} was modified in each of these simulations (to Hid^{313} or Hie^{313}) to preserve the hydrogen bond. Figure S2 shows the hydride-transfer and the proton-transfer distances along the MD simulations for the only two protonation states capable of a proton transfer. When a proton transfer to Hid^{502} was desired, only Hip^{546} produced structures capable of supporting the transfer. The combination of Hip^{546} and Hid^{502} produced a stable catalytic species where both the proton abstraction and the hydride-transfer distances were simultaneously optimal, as seen in Figure S2A. When the possibility for a transfer to Hie^{546} was considered, only the Hie^{502} could maintain an optimal proton-transfer distance. The combination of Hie^{546} and Hie^{502} produced the possibility for a proton transfer or a hydride transfer independently, but did not allow for a simultaneous transfer of both hydrogens (H^+ and H^-), as clearly seen when comparing both distances in Figure S2B. This last combination requires Glu^{389} to be deprotonated, in disagreement with the pK_a predictors. The other protonation states did not stabilize structures capable of a proton transfer to His^{546} or His^{502}, and later results showed that the enzymatic barrier is significantly higher when the hydride transfer must precede the proton transfer.

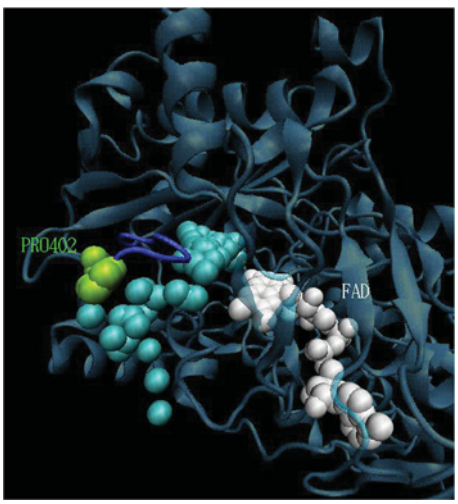

Figure S1 Methanol exit channel in AAO

PELE prediction of methanol migration trajectory, as a series of cyan van der Waals spheres, from the AAO active site, near the isoalloxazine ring of FAD (white spheres), to the protein surface. The 395–406 loop (dark blue) involved in this migration movement is indicated, including the position of Pro^{402} (green spheres).

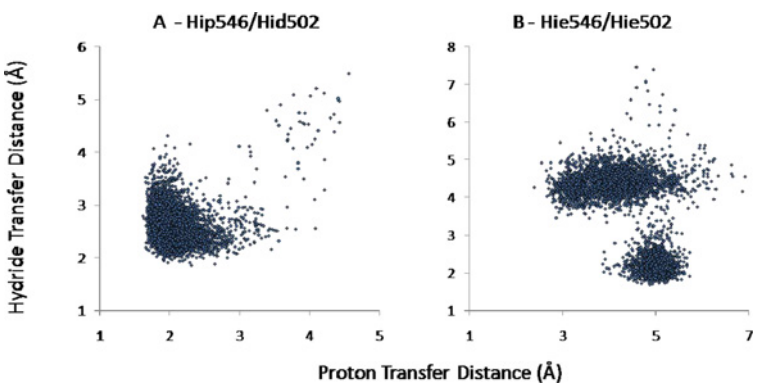

Figure S2 Histidine protonation studies

Proton- and hydride-transfer distances from the (*p*-anisyl) alcohol benzylic position to the histidine being able to act as catalytic base (His^{502} or His^{546}) and the flavin N-5 respectively, along 5 ns MD simulations (snapshots saved every 2 ps) considering two possible protonation states: (**A**) Hid^{502}/Hip^{546}, with His^{502} only protonated at Nδ and His^{546} doubly protonated; and (**B**) Hie^{502}/Hie^{546}, with both histidine residues being only protonated at Nε.

Received 14 December 2010/16 February 2011; accepted 4 March 2011
Published as BJ Immediate Publication 4 March 2011, doi:10.1042/BJ20102090

Medline/PubMed Citation | Related Articles in PubMed | Download to Citation Manager

Biochem. J. (2011) 436 (341–350) (Printed in Great Britain)

Substrate diffusion and oxidation in GMC oxidoreductases: an experimental and computational study on fungal aryl-alcohol oxidase

Aitor Hernández–Ortega*[1], Kenneth Borrelli†[1], Patricia Ferreira‡, Milagros Medina‡, Angel T. Martínez*[2] and Victor Guallar†[2]

*Centro de Investigaciones Biológicas, Consejo Superior de Investigaciones Científicas (CSIC), Ramiro de Maeztu 9, E-28040 Madrid, Spain, †Catalan Institution for Research and Advanced Studies, Barcelona Supercomputing Center, Edificio Nexus II, E-08028 Barcelona, Spain, and ‡Department of Biochemistry and Molecular and Cellular Biology and Institute of Biocomputation and Physics of Complex Systems, University of Zaragoza, E-50009 Zaragoza, Spain

[1]These authors contributed equally to this work.

[2]Correspondence may be addressed to either of these authors (email atmartinez@cib.csic.es or victor.guallar@bsc.es).

Movie S1 Ligand migration into the AAO active site: complete pathway

The movie shows PELE prediction of the complete migration pathway of *p*-anisyl alcohol (van der Waals spheres in CPK colours) from the protein surface to attain the active site in front of the *re*-side of the isoalloxazine ring of FAD (blue sticks) requiring important movements of several amino-acid side-chains (sticks in CPK colours).

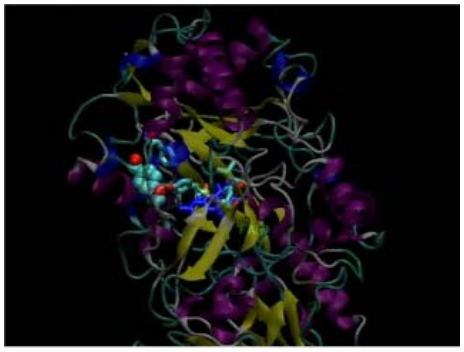

Movie S2 Detail of ligand migration into the AAO active site: side view

The movie shows a side view of the AAO active site and the details of PELE-predicted movement of *p*-anisyl alcohol (van der Waals spheres in CPK colours) to attain the active site in front of the re-side of the isoalloxazine ring of FAD (blue sticks). The side chains of active-site residues contributing to substrate migration movement (Tyr^{92}, Phe^{397}, Leu^{315} and Ile^{391}) and His^{502} involved in catalysis are shown (sticks in CPK colours).

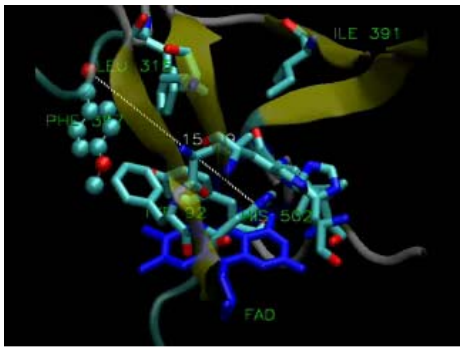

Movie S3 Detail of ligand migration into the AAO active site: front view

The movie shows a front view of the AAO active site (at the *re*-side of the isoalloxazine ring of FAD shown as blue sticks) and the details of PELE-predicted movement of *p*-anisyl alcohol (van der Waals spheres in CPK colours) to attain a catalytic position near the isoalloxazine ring with its hydroxy proton at 2.77 Å of Ne of His^{502}. The side-chain of His^{502}, and other active-site residues (Tyr^{92}, Phe^{397}, Leu^{315} and Ile^{391}) contributing to substrate migration movement, are shown (sticks in CPK colours).

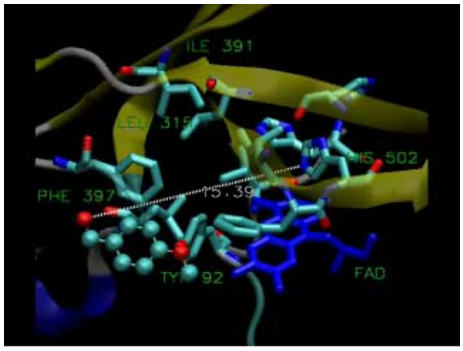

Received 14 December 2010/16 February 2011; accepted 4 March 2011

Published as BJ Immediate Publication 4 March 2011, doi:10.1042/BJ20102090